

Contents list available at CBIORE journal website

Renewable Energy Development

Journal homepage: https://ijred.cbiore.id



Research Article

Characterization of a geothermal system in the shallow structure of Seulawah volcano, Indonesia, using transient electromagnetic methods

Marwan^{1*}, Muhammad Yanis¹, Faisal Abdullah¹, Muhammad Ridha Adhari², Gartika Nugroho², Andri Yadi Paembonan³, Rinaldi Idroes⁴, Muhammad Yusuf⁴, Dian Budi Dharma^{5,6}, Muzakir¹, Deni Saputra⁷, Azman Abdul Ghani⁸

Abstract. Seulawah volcano, located in Sumatra, Indonesia, is renowned for its geothermal potential, a crucial source of cleaner energy for Indonesia's future growth and security. Available studies of Seulawah volcano primarily focus on its general geological, geochemical, and regional characteristics, with limited research on its shallow subsurface conditions. This study aimed to fill this research gap and enhance our understanding of the geothermal system of Seulawah volcano. There are two objectives of this study: (1) to conduct a transient electromagnetic (TEM) survey across the study area and (2) to better visualize and characterize the shallow subsurface conditions of the geothermal system of Seulawah volcano. The TEM method, which employed 60 stations (with distances between stations ranging from 0.5 to 1 km) and intersected several geothermal manifestations as well as local and regional faults, was used to achieve the objectives of this study. The Occam algorithm was applied for 1D inversion of TEM data, which was then validated using magnetotelluric data. The results of this study indicate that the geothermal system of Seulawah volcano has the potential to generate up to 230 Mwe of electrical energy. Moreover, the shallow depth (<200m) of Seulawah volcano is dominated by a resistive zone, which is interpreted to be related to the basaltic rocks of the Lamteuba Formation. The reservoir layer is located at depths of 200-500 m, exhibiting moderate resistivity values of >10 Ωm. At a depth of 500 m, a conductive layer with resistivity values <10 Ωm was observed, interpreted as a clay cap where fluids from the reservoir layer accumulate. Validation with magnetotelluric data shows results consistent with the TEM data, confirming that the findings of this study are reliable. These findings contribute to a deeper understanding of the geothermal system of Seulawah volcano and are expected to support the development of greener, renewable energy sources for Indonesia.

Keywords: transient electromagnetic, Seulawah volcano, geothermal, reservoir



@ The author(s). Published by CBIORE. This is an open access article under the CC BY-SA license (http://creativecommons.org/licenses/by-sa/4.0/). Received: 25th Oct 2024; Revised: 16th February 2025; Accepted: 19th March 2025; Available online: 27th March 2025

1. Introduction

Geothermal energy is an alternative renewable energy source that produces and supplies electrical power from the Earth's interior heat source of magma, where heat accumulates in the hot rocks beneath the surface at high temperatures (Moya et al., 2018). The total global geothermal power generation capacity reached 16.127 MWe by the end of 2022, an increase of 273 MWe compared to the 15,854 MWe installed capacity in 2021 (Hochstein & Sudarman, 2008). The United States of America remains the leading country in geothermal power generation, followed by Indonesia in second place in 2022 (Hochstein &

Sudarman, 2008). Indonesia is estimated to have geothermal energy potential amounting to 40% of the world's total, approximately 28,617 MWe. (Hochstein & Sudarman, 2008).

At least 20 potential geothermal fields are estimated to be located in the northernmost part of Sumatra. These include the Jaboi volcano on Weh Island, with an estimated power of 80 Mwe (Yanis, Ismail, et al., 2022), Geuredong and Burni Telong in Central Aceh (Nugraha et al., 2016; Yanis, Marwan, et al., 2022), Peut Sagoe in the Pidie region (Yanis et al., 2023; Yanis, Novari, et al., 2020; Zaini et al., 2022), and Seulawah Agam (Marwan, Yanis, et al., 2019; Zaini et al., 2021), with an estimated

¹Geophysical Engineering Department, Universitas Syiah Kuala, Darussalam-Banda Aceh 23111, Indonesia

²Geological Engineering, Universitas Syiah Kuala, Darussalam-Banda Aceh 23111, Indonesia

³Geophysical Engineering Department, Institut Teknologi Sumatera, Lampung, Indonesia

⁴Chemistry Department, Universitas Syiah Kuala, Darussalam-Banda Aceh 23111, Indonesia

⁵Energy and Mineral Resources Agency of Aceh Province, Banda Aceh 23114, Indonesia

⁶Graduate School of Mathematics and Applied Sciences, Universitas Syiah Kuala, Indonesia

⁷PT. Elnusa Tbk, Simatupang, Graha Elnusa, Jakarta Selatan 12560, Indonesia.

 $^{^{}g}$ Department of Geology, Faculty of Science, University of Malaya, 50603 Kuala Lumpur, Federal Territory Malaysia

electrical energy potential of 230 Mwe (Marwan, Yanis, et al., 2021). These potential geothermal fields, however, remain underexplored and undeveloped, likely due to the lack of government support and incentives. In the future, as the world transitions to greener and renewable energy sources, these geothermal potentials could serve as a substitute for today's ubiquitous fossil fuels (oil, gas, coal, etc.).

This research focuses on the geothermal potential of Seulawah Agam volcano, located in the Province of Aceh, Sumatra, Indonesia. Over the last two decades, numerous studies have been conducted to understand the large-scale dynamics of the Seulawah Agam volcanic geothermal area, which has an estimated energy potential of 230 Mwe (Marwan, Yanis, et al., 2019; Nasruddin et al., 2016). These earlier studies include geochemical investigations aimed at understanding the geothermal water sources and predicting temperatures at several surface manifestations (Idroes et al., 2019). Moreover, several integrated geophysical surveys have also been carried out, including the magnetotelluric (MT) method (Marwan, Yanis, et al., 2019, 2021), as well as remote sensing studies such as the use of Landsat series data to monitor thermal activity from 2010 to 2020 (Zaini et al., 2021), and the use of UAV data for thermal monitoring with higher resolution (Marwan, Idroes, et al., 2021).

Most of the studies mentioned above were conducted on a regional scale using the MT method. However, the local subsurface structure models and some manifestations cannot be adequately described using the MT method, as its low-frequency depth penetration can only explain deep anomalies with low resolution. Therefore, we have decided to use the transient electromagnetic (TEM) method to characterize volcanic layers in shallow areas and to overcome the limitations of the MT method.

This study aims to improve the existing conceptual model of the Seulawah geothermal system using high-resolution TEM data and to identify the subsurface fluid pathways within the system. It is the first geophysical survey of the study area to focus on shallow depths (<1 km) at a local scale around geothermal manifestations and hydrothermal deposits, which typically exhibit high electrical resistivity (Ruiz-Aguilar *et al.*, 2020). There are two objectives of this research: (1) to conduct a transient electromagnetic (TEM) survey across the study area and (2) to better visualize and characterize the shallow subsurface conditions of the Seulawah volcanic geothermal system.

2. Literature Study

2.1 Geological Setting of Seulawah Volcano

Seulawah volcano is primarily composed of the Lamteuba Formation, as shown in Fig. 1. This Formation consists of lava and pyroclastic rocks, ranging from basaltic to andesite and dacitic rocks, as well as volcanic breccias, tuff, and agglomerate. Furthermore, the study area includes other rock types, such as alluvium, sandstone, conglomerate, limestone, and the Indrapuri Formation (Bennett *et al.*, 1981). Several geothermal manifestations are present within the study area, including hot springs, warm ground, and craters (Idroes *et al.*, 2019; Marwan, Syukri, *et al.*, 2019). The hot springs are located in Ie Jue, Ie Busuk, Ie Seu'um, Alue Utuen Pineung, Alue Pu, Ie Masam, and Alue Tungku.

Generally, the volcanoes in Sumatra are controlled by the regional fault systems of the Great Sumatran Fault (Hochstein & Sudarman, 1993; Saptadji, 2001), which extends 1700 km from Lampung to the Andaman Archipelago in India (Rizal *et al.*, 2019; Sieh & Natawidjaja, 2000; Yanis, Faisal, *et al.*, 2020). This fault is divided into 20 segments, two of which are located at the northern tip of Sumatra: the Aceh segment, which extends to Aceh Island, and the Seulimum segment, which leads to Weh Island (Abdullah *et al.*, 2022; Marwan, Asrillah, *et al.*, 2019; Yanis, Abdullah, *et al.*, 2021). Seulawah Agam is one of the

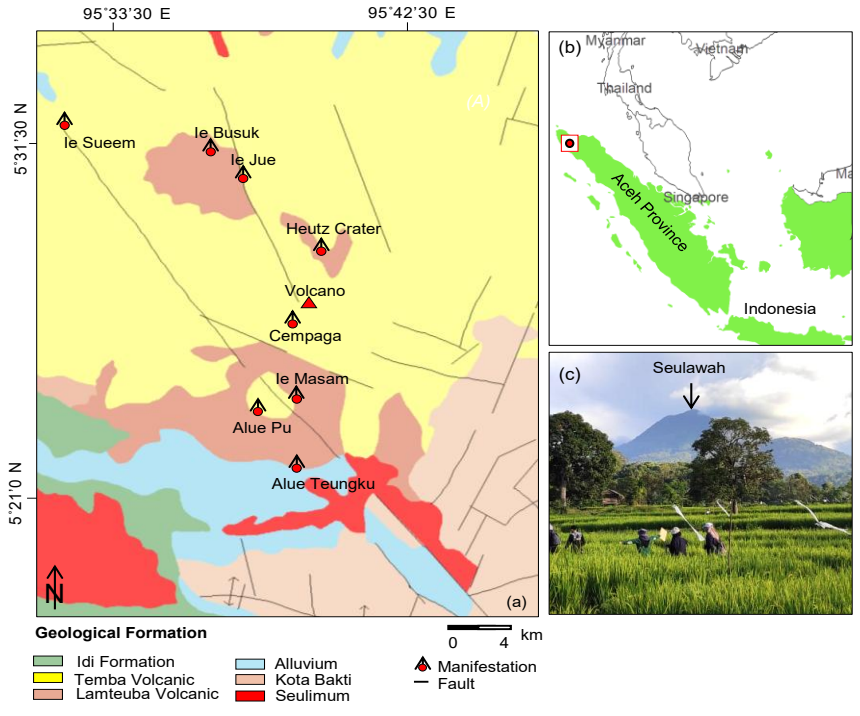


Fig 1. (a). Geological map of the Seulawah volcano, which is generally dominated by Lamteuba volcanic formation. This map was adopted from regional geological maps (Bennett et al., 1981), where (b) shows the location of the volcanoes at the northern tip of Sumatra Island in Aceh Province, while (c) is photographic documentation showing the high topography of one of the volcanoes, reaching up to 1700 m.

active volcanoes in Aceh Besar District, Aceh Province, in the north of Sumatera, Indonesia. This volcano was formed due to the tectonic activity of the Sunda megathrust on the east side of Sumatra Island, as shown in Fig. 1 (Hochstein & Sudarman, 1993; Marwan, Syukri, et al., 2019; Yanis, Marwan, et al., 2021).

In addition, the subduction zone along the west coast of Sumatra, at a depth of 100 km, has also caused shallower magnetization, with geothermal reservoir rocks typically found in sedimentary rocks. These fault systems may have provided a migration pathway for fluids, connecting them to the geothermal system of Seulawah Agam. Moreover, many surface geothermal manifestations are located near these fault systems, providing evidence of the close relationship between the fault systems and the geothermal system.

The study area is primarily composed of the Lamteuba Formation (Fig. 1). This formation consists of lava and pyroclastic rocks, ranging from basaltic, andesite, and dacite to volcanic breccias, tuff, and agglomerate. Furthermore, the study area contains other rock types, such as alluvium, sandstone, conglomerate, limestone, and the Indrapuri Formation (Bennett et al., 1981). Several geothermal manifestations are found within the study area, including hot springs, warm ground, and craters (Idroes *et al.*, 2019; Marwan, Syukri, *et al.*, 2019). The hot springs are found at Ie Jue, Ie Busuk, Ie Seu'um, Alue Utuen Pineung, Alue Pu, Ie Masam, and Alue Tungku (Fig. 1).

2.2 Basic Theory of Transient Electromagnetic

Electromagnetic (EM) methods are geophysical techniques that measure electric and magnetic fields to obtain conductivity parameters from subsurface layers. (Ruiz-Aguilar et al., 2020; Yanis et al., 2017, 2019). Two different domains in EM methods are the time domain EM (TDEM) method, also called transient electromagnetics (TEM), and the frequency domain electromagnetics (FDEM). The TDEM method involves generating transient electromagnetic fields using a transmitter coil and measuring the resulting induced electromagnetic fields with a receiver coil. The transmitter coil is energized with a short pulse of current, typically lasting a few microseconds. The resulting transient EM field propagates through the subsurface and induces eddy currents in the conductive subsurface materials. The induced currents, in turn, generate secondary EM fields that are detected by the receiver coil. The response of the subsurface materials to the transmitted EM fields provides information about the subsurface geology (Nabigian, 2008; Chave and Jones, 2012; Vozoff, 1980). Faraday's principle of induction states that a rapidly changing current in the primary field induces eddy currents in the surrounding conducting medium (Vozoff, 1980). The transient of the EM field (H_0) step function at the time t=0 is expressed as

$$e_{x}(z,t) = \frac{2H_{0}}{\sigma} \sqrt{\frac{\sigma\mu}{2t}} e^{-(\frac{\sigma\mu}{2t} + \frac{z^{2}}{2})}$$
(1)

and

$$h_{y}(z,t) = 2H_{0} \operatorname{erfc}(\sqrt{\frac{\sigma\mu}{2t}} \frac{z^{2}}{2})$$
 (2)

where σ represents the conductivity (S/m), μ denotes magnetic permeability, t is time (s), and z indicates the depth (m) (Nabigian, 2008).

The measurement begins after the transmitter current is turned off; the current loop can be thought of as an image of the transmitter loop in the ground. Due to the finite ground conductivity, the current begins to decay immediately, which in turn induces a voltage pulse that drives more current to flow. The time-dependent response is measured using a multi-turn

receiver coil. The time derivative of the vertical magnetic flux density $(\mathbf{B}_z = \mu_0 \mathbf{H}_z)$ is equal to the voltage induced in the receiver coil, V(t), divided by the receiver coil moment M_{Rec} (McNeill, 1980). The receiver coil moment is the product of the coil receiver area and the number of cables in the coil. Therefore, the measured EM response can be mathematically represented as (Fitterman & Stewart, 1986):

$$\frac{V(t)}{M_{Rec}} = \frac{\mu M_{Trans}}{5t} \left| \frac{\mu}{4\pi t \rho} \right|^{3/2} \qquad , \tag{3}$$

where the resistivity of half the surface space is $\rho = 1/\sigma$ and M_{Trans} denotes the transmitter loop moment (M = AI for square loops, where A is the area of the transmitter loop and I is the transmitter current).

The initial time equation can be algebraically can be inverted to obtain the apparent resistivity value, as shown in eq4:

$$\rho_{a (t)} = \frac{\mu}{4\pi t} \left| \frac{2\mu M_{Trans}}{5tB_{\tau}} \right|^{2/3} \tag{4}$$

Alternatively, when considering the receiver moment, the equation becomes

$$\rho_{a(t)} = \frac{\mu}{4\pi t} \left| \frac{2\mu M_{Trans} M_{Rec}}{5tV(t)} \right|^{2/3} , \qquad (5)$$

where ρ_a represents the resistivity value, assuming the field is detected using the vertical axis coil (McNeill, 1980; Fitterman and Stewart, 1996; Zhdanov, 2009). The data obtained from the field must be processed before inversion. Finally, after processing, including noise filtering, stacking, and smoothing to obtain data with a high signal-to-noise ratio (SNR), the apparent resistivity value is determined using eq.5. Data modeling from the TEM method is performed through the application of 1D inversion, where the Occam algorithm is one of the commonly applied source codes (Strack, 1992).

3. Methodology

3.1. Design Survey of TEM Data

One unit of TEM system typically consists of a source loop and a receiving loop. An inductive cable, embedded below the surface, serves as the source to generate an EM field, which is transmitted to the subsurface through the current flow in the wire. The receiver captures the time derivative of the secondary magnetic field. Specifically, the layer resolution and depth of the anomaly are influenced by the loop size and the magnitude of the transmitted current. To study the geothermal system and caldera margin of the volcano, all data points are measured to cover the volcanic area. A total of 60 measurement stations are distributed across the volcanic areas, with a distance of 500 m between points, in order to obtain a reasonable resolution of the model. The arrangement of the cable loops forms a square with a side length of 100 m. The design of the measurement survey is illustrated in Fig. 2a.

Each station employed a low moment and a high current of up to 40A, with a switching time of 0.8–80 ms. Therefore, data points were also obtained in several manifestation areas, such as in the craters of Heutz, Cempaga, Ie Suum, and many other features. Based on the distribution of the TEM stations, a cross-section for the 2D model with 9 profiles was created. These profiles cross regional faults from the GSF and local faults from

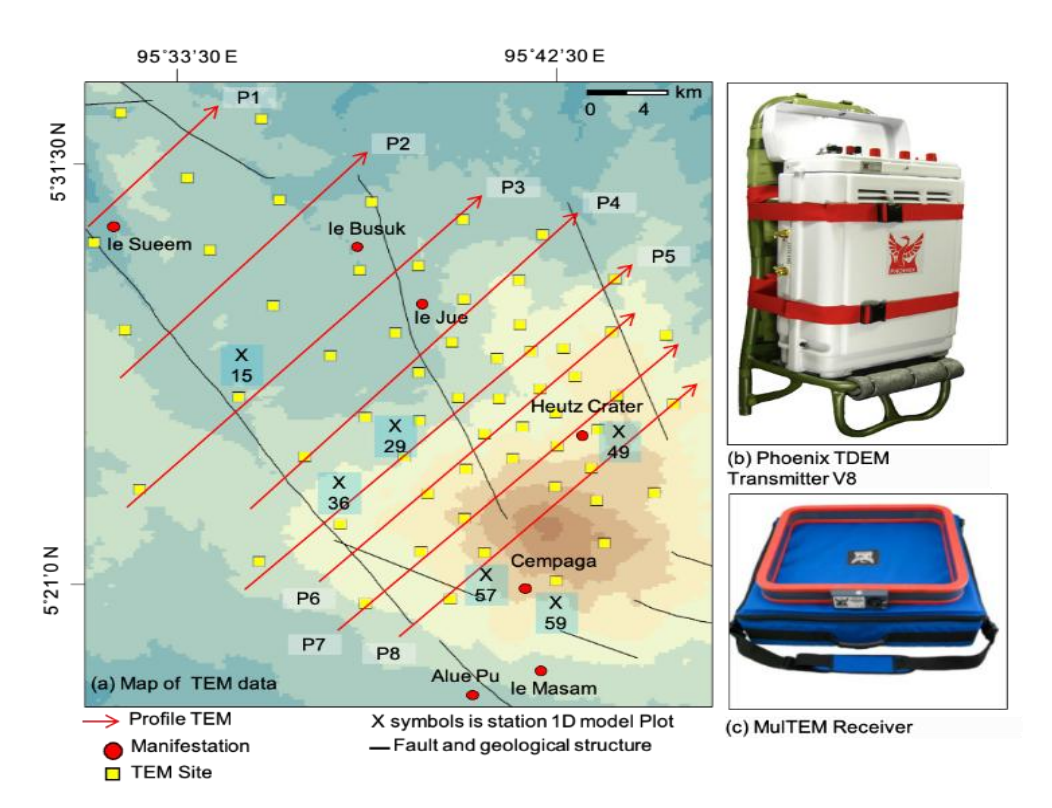


Fig 2. Topographic map of the 60 TEM data points and 9 profiles, which were obtained from the entire station, illustrating regional and local faults as well as some manifestations such as the Heutz and Cempaga craters. The symbol P represents the TEM profile, and the symbol 'x' denotes the 1D data points, which are plotted to explain the depth of the resistivity layer. Panel (b) shows the Phoenix RXU-TMR and T-4 Transmitter, while panel (c) displays the receiver loop model used in this study, the MulTEM-AL, developed by Phoenix Corporation of

volcanoes in the NW-SE direction. The profiles were used to study the relationship between regional and local faults and volcanic systems, which may serve as access points for rising fluids to the surface. For example, the P1 profile crosses the regional fault and the Ie Suum manifestation, the P2-P3 profile covers the Ie Busuk manifestation, and the P5-P8 profiles cross the Heutz crater, Ceumpaga, and several other local faults. The Phoenix RXU-TMR and T-4 Transmitter were used in this research. They can operate with turn-off times as short as half a microsecond, allowing for maximum resolution of near-surface anomalies, as depicted in Fig. 2b. The Multem Receiver was used as the receiving instrument (Fig. 2c). The output current generated by the transmitter can reach up to 40 A, proving a strong response and high resolution to depths of up to 500 m, making it an ideal instrument for resistivity sounding over a wide area.

3.2. Data Processing

Occam is an inversion algorithm introduced by Parker and Constable in 1987, based on the principle that allows for continuous resistivity variations with depth (Hördt *et al.*, 1992). The Occam inversion provides a smooth resistivity model with a minimum target misfit value. This inversion typically yields realistic and smooth results when applied to resistivity structures. (Li *et al.*, 2015). The thickness of the Earth's layer in the Occam inversion is considered equivalent to the distance in logarithmic space. Unlike traditional least-squares inversion, the Occam inversion demonstrates the best-fitting smooth model. To represent and understand our data, we typically require a preferred model, even though inverted electromagnetic data is

known to be nonunique. It is advisable to avoid incorporating characteristics that are not truly necessary for the data and to ensure the model is independent of the number of layers or the initial model selected (Li *et al.*, 2015).

The Earth model in this inversion is constructed continuously based on the horizontal layer approach, which is mathematically expressed by eq.6:

$$U = \mu^{-1} (\chi^2 - \chi^{*2}) + R , \qquad (6)$$

where the Lagrangian function is denoted as μ , the misfit value is symbolized as (χ^*) , and the chi-square error (χ^2) is the calculation between the calculated data and the measured data, as expressed in eq.7:

$$\chi^2 = \sum_{i=n}^{n} \left(\frac{d_{i-f_i(m)}}{\sigma_i}\right)^2 \quad , \tag{7}$$

where n represents the number of data points at the measured locations $(d_1...d_n)$, with the corresponding standard deviations $(\sigma_1 ... \sigma_n)$. The calculation data $(f_1(m) ... fn)$ depends on the model vector $m_1 ... m_n$, which varies based on the resistivity values and the layer thickness. Specifically, the Occam inversion equation can be adjusted as shown in eq.7:

$$U = \mu^{-1} \left\{ \left\| \widetilde{\mathbf{W}} \mathbf{d} - \widetilde{\mathbf{W}} \widetilde{\mathbf{G}} \mathbf{m} \right\|^{2} - \chi^{*2} \right\} + \left| \widetilde{\mathbf{0}} \mathbf{m} \right|^{2}. \quad (8)$$

For each μ value that does not change, the value of the gradient U with respect to m will be removed, so that the model form (m) of the Occam inversion is mathematically shown by eq.8:

$$\mathsf{m} = \left[\mu \partial^{\mathsf{T}} \partial + (\widetilde{W}\widetilde{\mathsf{G}})^{\mathsf{T}} \widetilde{W}\widetilde{\mathsf{G}} \right]^{-1} (\widetilde{W}\widetilde{\mathsf{G}})^{\mathsf{T}} \widetilde{W} d \quad . \quad (9)$$

Variations in the value of μ produce the true model shape. The value of μ must be determined such that the misfit value can be known (Constable *et al.*, 1987; Siripunvaraporn & Egbert, 2009; Yanis, Marwan, *et al.*, 2022).

A one-dimensional Earth model can be obtained using the Occam inversion code developed by Constable *et al.* (1987) to produce a precise solution for the subsurface 1D structure. TEM-sounding curves provide information about the general structure, which may be expected from subsequent 2D and 3D modeling. The filtered apparent resistivity data and time are used as input parameters in the inversion, assuming five resistivity layers based on the initial standard model and a depth of 100 to 1000 m (Telford *et al.*, 1990). Additionally, the provided homogeneous half-space resistivity parameter value is set to $100 \Omega \text{m}$, with 10 iterations, and errors assessment reveals a root mean square (RMS) value limit of 6.5%.

4. Result and Discussion

4.1 1D Inversion of TEM Data

Fig. 3 shows examples of 1D TEM data inversion results using the Occam algorithm, which focuses on locations directly influenced by volcanic activity, including regional and local manifestations, as well as fault areas. At site 49 (Fig. 3a), near the crater, the resistivity values vary with depth up to 1 km below the surface. At depths between 0 and 200 m, the obtained resistivity values are relatively high (26.13 m). This shows a

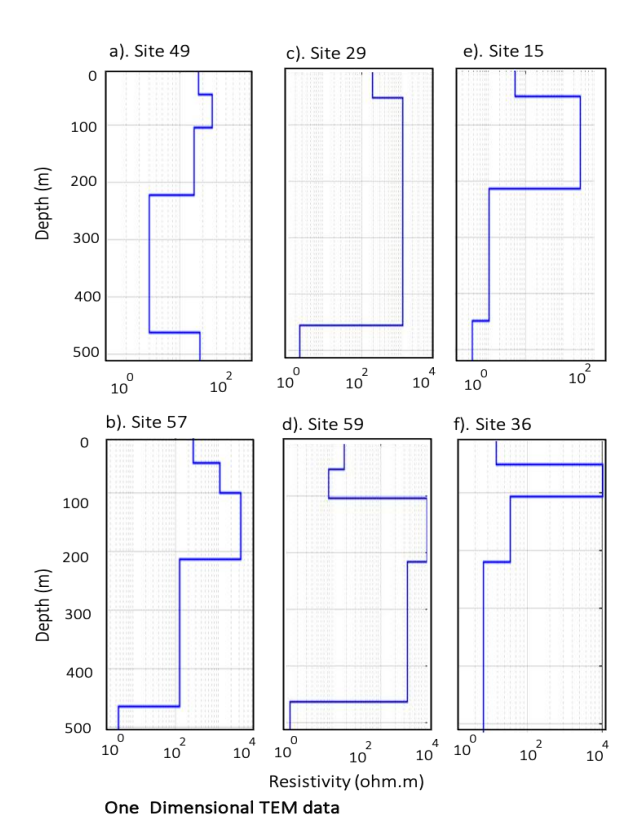


Fig 3. Some examples of 1D TEM data models processed using the Occam algorithm for all stations: (a) station 49 and (b) station 47, which is close to the volcanic manifestation, (c) station 29, and (d) station 59, which is located at the caldera margin area of Seulawah, while (e) station 15 and (f) station 36, which are close to the regional fault of the Seulimum segment and local faults near the volcano.

response from the resistive layer, which is believed to be a basaltic layer or volcanic deposit near the Heutz crater. This rock is classified as the Lamteuba Formation, part of an extrusive igneous rock that has cooled at the Earth's surface, and it is the dominant volcanic rock mostly found in tropical areas (Wang $et\ al.,\ 2018$). Furthermore, at depth of 200 to 400 m, a conductive anomaly with a value of 3.94 Ωm is obtained. This represents a response from the clay cap layer, which acts as a reservoir for fluid accumulation. If a fault is present, then the fluid in this layer will rise to the surface, forming surface manifestations.

In another manifestation, site 57 is located at the Cempaga crater (Fig. 3b), where a similar layer model was obtained at the previous manifestation site. A resistive anomaly was observed, which corresponds to the basaltic layer covering the fluid in the clay cap. This fluid can also be traced at depths between 200 and 400 m, where it exhibits low resistivity. These results show that the reservoir in the Cempaga crater area is much deeper than that in the Heutz crater. In other locations near the volcano, such as sites 29 (Fig. 3c) and 59 (Fig. 4d), similar resistivity layers are found as in the crater areas, but at different depths. This is due to volcanic activity, although there are no specific volcanic manifestations. For example, in the first layer, a resistive layer is obtained to a depth of 0-400 m, which is suspected to be a volcanic base layer. A conductive layer is then suspected to be a caprock at depths between 400 and 500 m below the surface.

At a location close to the fault, such as at site 15 (Fig. 3e), the results of the Occam 1D inversion show that the first layer is very resistive and then becomes conductive at the same depth as the TEM point near the crater. This behavior is due to the location of the point within the regional GSF area, meaning that in the near-surface region, the resistivity is not significantly affected. Therefore, the inversion data only visualizes the resistivity changes due to volcanic activities. Meanwhile, at the local fault location, site 36 (Fig. 4f), a high resistivity value is found at a depth of less than 200 m, which then changes to become highly conducive at a depth of 500 m. This change in conductivity is caused by volcanic activities and the presence of a local fault, which is also the main controller of the Seulawah geothermal system. To examine the full extent of the TEM data, cross-sectional profiles were created, covering manifestations, volcanoes, and regional and local faults.

The 1D inversion of TEM data has revealed the geometry of the Seulawah Agam geothermal system, especially in shallow areas. The data is also validated with magnetotelluric measurements, which is an effective method used in geothermal studies. The results of this 1D inversion provide information only on the variation in resistivity with depth. Therefore, a pseudo-2D visualization is created to describe the overall mechanism of the geothermal system. The first layer is dominated by a resistive zone, which corresponds to basaltic rock reaching depths of 0 to 200 m. Below this, a conductive clay cap layer is located at depths between 200 and 500 m, while a moderately resistive reservoir layer is identified at profile 4, between 400 and 500 m, and is interpreted as the reservoir. Additionally, several 2D cross-sections map the presence of regional and local faults, which are key mechanisms in the formation of geothermal elements in volcanic areas. These faults act as conduits, transporting fluids from the clay cap layer to the surface, creating manifestations such as Ie Jue, Ie Suum, Heutz, and Cempa craters.

According to previous studies (Hochstein & Sudarman, 2008; Nasruddin et al., 2016), several models of geothermal reservoirs exist, including hydrothermal systems that contain

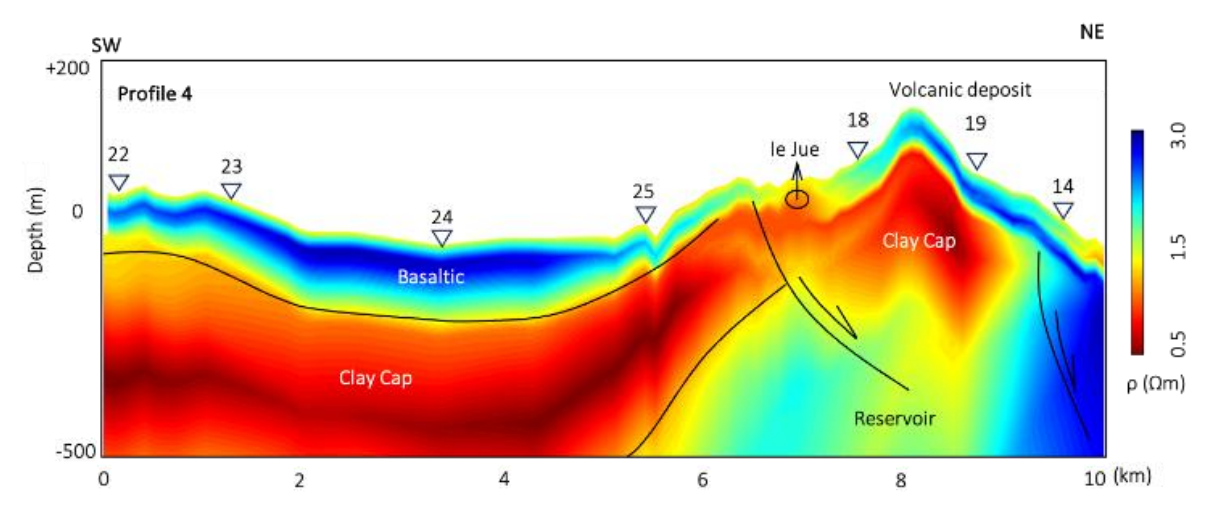


Fig 4. 2D pseudo-cross-section model in profile 4 spans across the manifestations of the Ie Jue volcano. This model was derived from the analysis of the Occam 1D algorithm. The clay cap zone exhibits a strong contrast with high conductivity at 100–500 m depth.

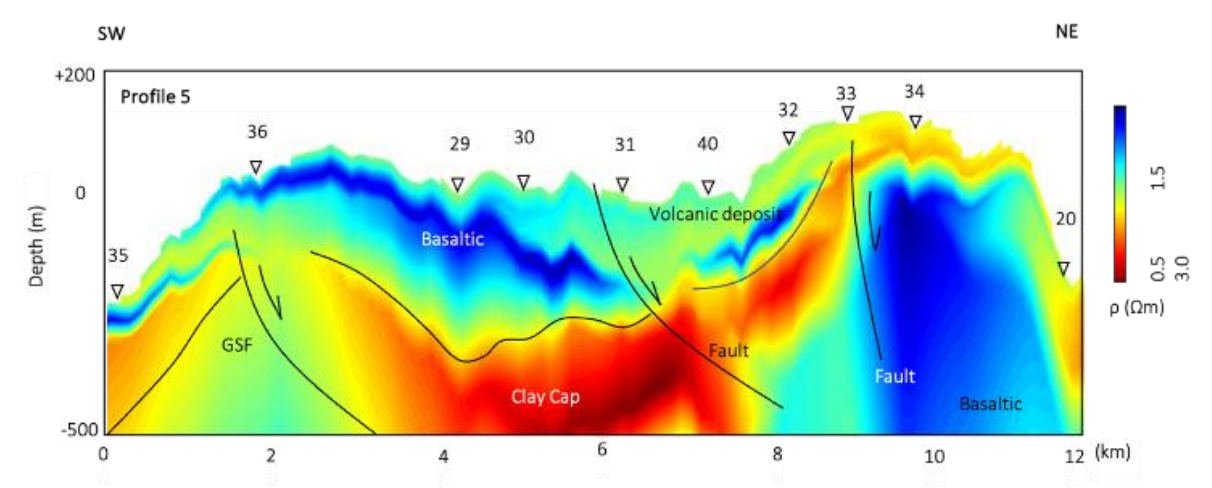


Fig 5. 2D cross-section model in profile 5 is measured across regional faults from the GSF and local faults, the main mechanism for controlling fluid in the volcano. The conductive zones, likely representing faults, can be seen clearly at 2, 6, and 9 km from the measurement path.

fluids in the form of gas, liquid, or a mixture of both, depending on the pressure and temperature within the reservoir. In addition, there is the hot dry rock system, which does not contain steam and water; the operation of this system requires injection and production wells to produce fluid that flows through the hot dry rock (Purnomo & Pichler, 2014). Therefore, understanding the presence of faults in volcanoes is crucial for geothermal development, as faults serve as pathways for fluid to enter and exit (Rybach, 2003; Yanis, Ismail, et al., 2022). However, in some areas dominated by resistive rocks, such as basalt, at the surface, fault activity may not bring fluids to the surface, preventing the formation of manifestations in those area. A 1D analysis of TEM data also shows that the resulting resistivity pattern is consistent with many of the world's geothermal systems (Ledo et al., 2021; Ruiz-Aguilar et al., 2020), where there is a high resistivity permeability layer and a lowresistivity clay cap covering the reservoir with more resistive, high-permeability zones.

4.2 Pseudo-2D Visualization of TEM data

Pseudo-2D analysis was performed on all TEM profiles that cross faults and volcanic manifestations. However, for the

geothermal generation system, we only presented three profiles, such as Line 4, which crosses the Ie Jue manifestations, as illustrated in Fig. 4. The overall length of the track is 10 km, with 7 TEM station data varying between 1 and 2 km. This line passes through manifestations of hot springs and several local faults that control the volcanic system. The results of this pseudo-2D cross-section show a resistive zone between 0 and 6 km, with resistivity values ranging from 280.63 to 2542.4 Ωm , and a thickness of 200 m below the surface. This anomaly is predicted to be a basaltic layer that inhibits fluid flow to the surface. The same resistive zone is also found on the east side, near the volcano's peak, with a resistive log of 3 Ωm .

This basaltic layer prevents the formation of manifestations along the volcanic zone. However, at a distance of 7 km from the measurement line, a conductive layer is obtained with resistivity values ranging from 2.12 to 12.04 m. This anomaly extends along the trajectory at a depth of 500 m, which is suspected to be a clay cap layer acting as a permeability shield of the fluid in the reservoir below. This fluid rises to the surface due to a local fault, which provides a pathway from the clay cap area. The fault can be mapped clearly at a depth of less than 500 m, directly beneath the Ie Jue manifestation, as

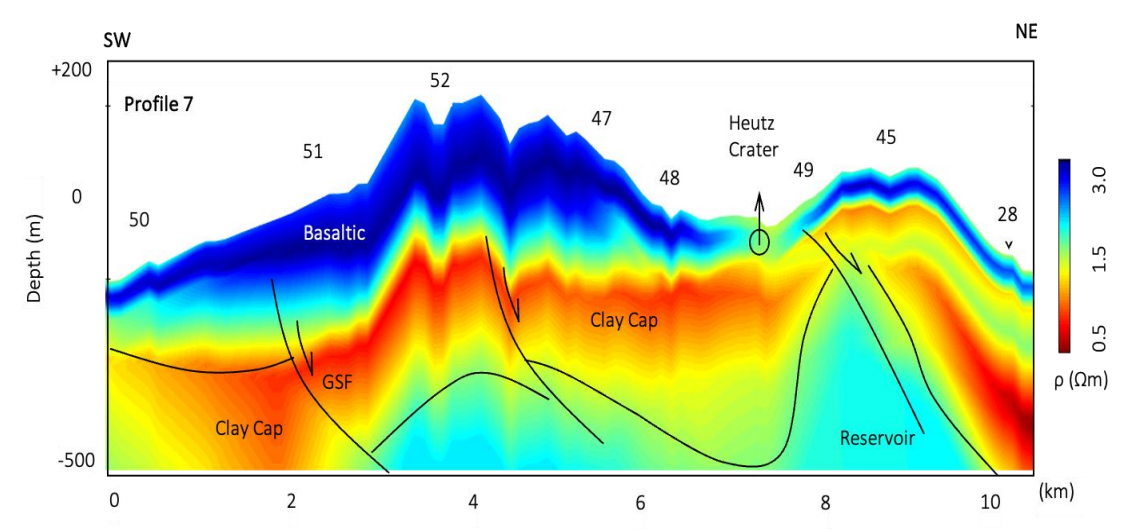


Fig 6. Pseudo-2D cross-section model on profile 7 measured across the Heutz crater and several faults from the volcano. At 8 km, a conductive zone is obtained which is thought to be a fault serving as the medium for accessing the fluid to the surface.

indicated by the geological map (Bennett et al., 1981). Additionally, at a depth of 500 m in the volcanic area, there is also a conductive zone, which is thought to represent the continuation of the clay cap. Due to the volcanic deposit layer, the fluid cannot penetrate to the surface, preventing manifestations in the area. Moreover, a moderate resistivity value was obtained to the NE of the volcano, with the anomaly extending to a depth of 200 to 500 m. This is suspected to be a reservoir layer, which is crucial for geothermal drilling.

On the east side, the high-resistivity anomaly is thought to represent the basaltic layer of the volcano, but further inversion is required, as the area is only represented by one TEM station. Profile 5, as shown in Fig. 6, crosses several regional and local faults. Overall resistivity values range from 1.09 to 1935.4 Ωm . At a distance of 0 to 9 km from the high-resistive zone, the resistive layer, with values ranging from 185.71 to 1935 Ωm and extending to a depth of 300 m below the surface, is suspected to be a basaltic or volcanic deposit that hinders fluid access. At a depth of 500 m on the west side, there is a conductive layer. Between 3 and 9 km, the conductive layer extends to a depth of 1 km and is suspected to be an anomaly related to the clay cap, which accumulates geothermal fluid.

One factor contributing to the separation of this conductive zone at a distance of 2 km is the presence of the Seulimum segment of the GSF, which is also responsible for controlling the geothermal mechanism in the volcano. In addition, local faults are clearly visible at distances of 6 km and 10 km from the measurement line (Fig. 1). While there are many faults in the area, the fluid in the clay cap layer cannot rise to the surface because the base layer is dominated by dense resistive zones, such as basaltic rock. This prevents the formation of manifestations in the area. Even near the surface, at a distance of 8 km, the resistive zone, suspected to be a volcanic deposit, can be mapped clearly. At a depth of 500 m, a moderate resistive value ranging from 25.75 to 116.32 Ωm was observed. This layer is suspected to be a geothermal reservoir for storing and circulating thermal fluids, such as steam or hot water. This area represents a sought-after anomaly for geothermal production, as the hot fluid can drive turbines to generate electrical energy (Hartono et al., 2020; Hochstein & Sudarman, 1993).

A 2D pseudo-cross section of profile 7 was measured across the Heutz fault and crater, as illustrated in Fig. 6. In this line, the

resistivity values ranged from 0.5 to 1750 Ωm to a depth of approximately 500 m below the surface. In volcanic areas with high topography, dominated by basaltic rock with high resistivity (187.85 – 1750 Ωm), this zone can be mapped at a depth of 500 m, extending from 0 to 7 km from the measurement profile. The same anomaly is also found on the eastern side of the volcano, in the lower topography.

While at a depth of 200-500 m, a conductive layer with low resistivity values ranging from 0.56 to 15.75 Ω m is obtained. This anomaly is thought to be a response to the clay cap area, which covers the hydrothermal flow from the reservoir. The fluid contained in the clay cap layer cannot rise to the surface, even though faults exist in some locations, such as the Seulimum segment at a distance of 2 km and a local fault of 5 km. This is due to a thick basaltic layer, extending up to 300 m, which prevents the formation of manifestations. Meanwhile, in areas without a basaltic layer, such as at a distance of 7 km, surface manifestations are observed at the Heutz crater, where fluid rises through the local fault that controls the area. This fault is also clearly visualized in the results of the Occam 1D inversion. Overall, the TEM data cross-section model has provided valuable information about the geothermal system in shallow structures. The model offers insights into basaltic layers near the surface, clay cap layers, reservoirs, and the faults that control the volcano.

4.3 Pseudo-3D Analysis of TEM

To study the existence of various geothermal systems at different depths, we analyzed the depth slice model of Occam's 1D inversion result (Fig. 7). For example, at a depth of 0–100m (Fig. 7a), which characterizes the surface area of the measurement site, a conductive value with resistivity of less than log 1.5 Ωm is observed. This anomaly is primarily concentrated on the north side, corresponding to the activities of several manifestations, such as Ie suum, Ie Busuk, and Ie Jue. In addition, the area is dominated by conductive anomalies near the volcanoes, including the Heutz crater. However, the dense basaltic layer with high resistivity (greater than log 2 Ωm), which focuses on the volcanic surroundings, makes the 1D TEM model response insensitive to conductive changes in the Cempaga crater.

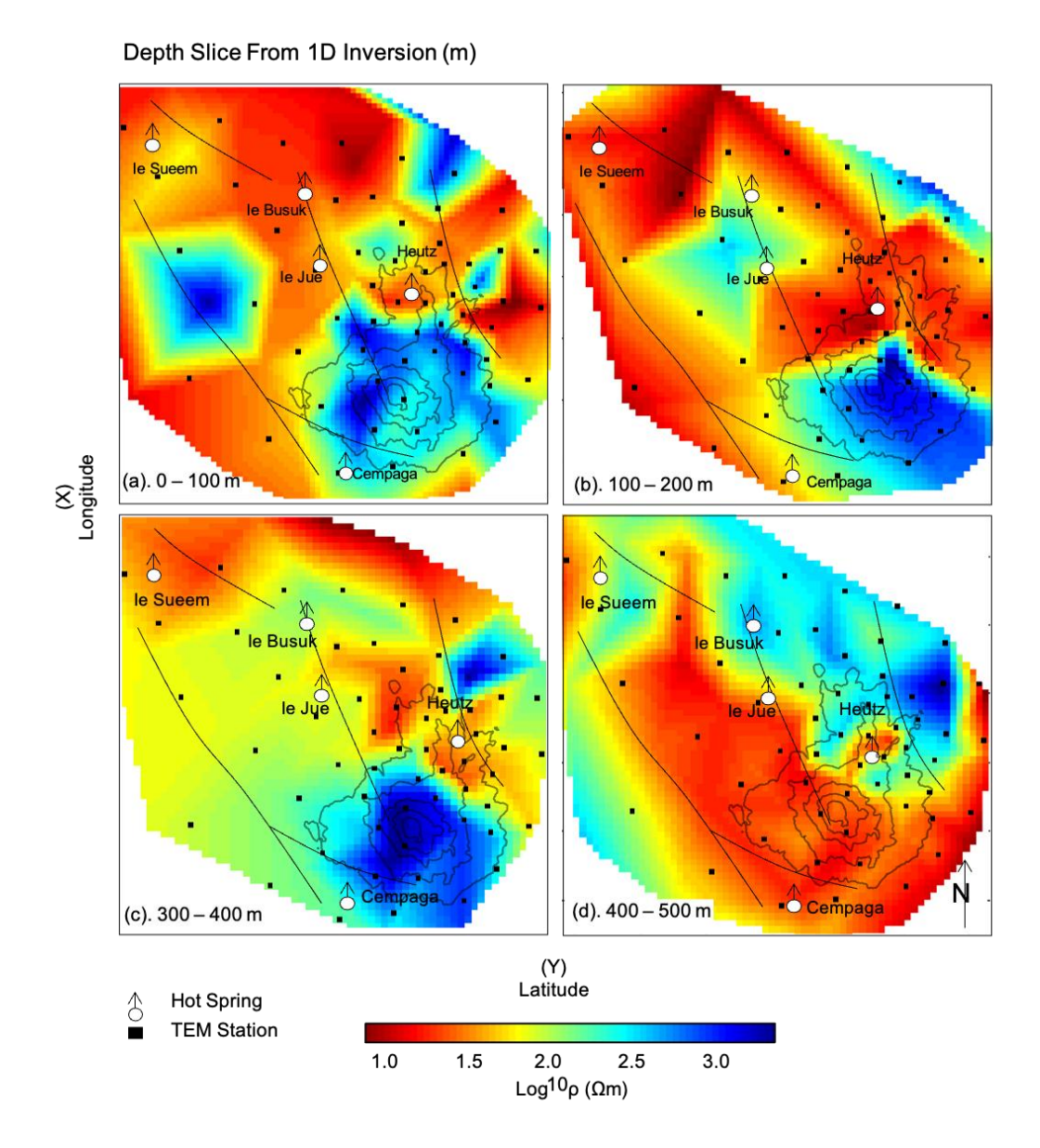


Fig 7. Depth slice of 3D resistivity combined from the results of the 2D inversion model on several paths. This 3D model is sliced at various depths ranging from (a) 0–100 m, (b) 100–200 m, (c) 300–400 m, and (d) 400–500 m, for mapping fractures and hydrothermal flows in volcanoes. Geological faults are shown as black lines (Bennett et al. 1981), and the distribution of TEM points is indicated by black dots.

The impermeable basaltic layer also inhibits fluid flow from the clay cap area, preventing the formation of manifestations. Additionally, some local faults near the Heutz crater can be mapped clearly, while the regional faults of the GSF do not significantly affect the resistivity values at this shallow depth. GSF tectonic activity generally forms several local faults in the SE–NW direction in the Seulawah area.

These faults are associated with a low-resistivity anomaly, which can be interpreted as a channel that transports thermal energy from the heat source to the surface (Peacock et al., 2016). Therefore, some low-contrast anomalies with multiple conductors are closely related to local faults and fractures from Seulawah Agam. At a depth of 100–200 m (Fig. 7b), the same anomaly observed at the previous depth was found, with a conductive anomaly appearing in the crater, indicating volcanic activity or a suspected hydrothermal area.

At a depth of 300-400 m (Fig. 7c), a conductive anomaly is observed on the west side of the volcano. This may be due to the clay cap layer covering the thermal fluid from the reservoir. Clay caps serve as good indicators of an underlying hightemperature geothermal reservoir in high-temperature geothermal fields, acting as a reservoir seal to prevent the loss of hot liquid to the atmosphere (Lichoro et al., 2017). Furthermore, at depths between 100 and 400 m, the conductive anomalies clearly map the presence of Seulawah volcanic manifestations, such as the Heutz and Cempaga craters, while the presence of regional faults from the GSF can also be visualized. This indicates that, in addition to the local fault, the Seulimum segment also plays a crucial role in controlling the geothermal system on the Seulawah volcano. At a depth of 400 to 500 m, a more conductive anomaly is obtained, which corresponds to a reservoir with high porosity and permeability. This anomaly is traced on the northeast side of the volcano and

Table 1	
Results of the geochemical analysis of geothermal water (in units of 1. mg.L ⁻	·1)

Location	Code	K ⁺	Na ⁺	Mg^{2+}	Ca ²⁺	Li+	B ⁺	Cl-	SO ₄ ² -	HCO ₃ -
Ie Masam	IM	20.21	77.02	62.18	113.84	0.11	0.681	20.25	77.52	602.80
Alue PU	PU	10.07	50.02	34.47	53.17	0.05	0.440	10.47	49.75	401.38
Alue Teungku	AT	8.30	48.52	33.86	79.03	0.01	0.892	8.37	48.56	384.15

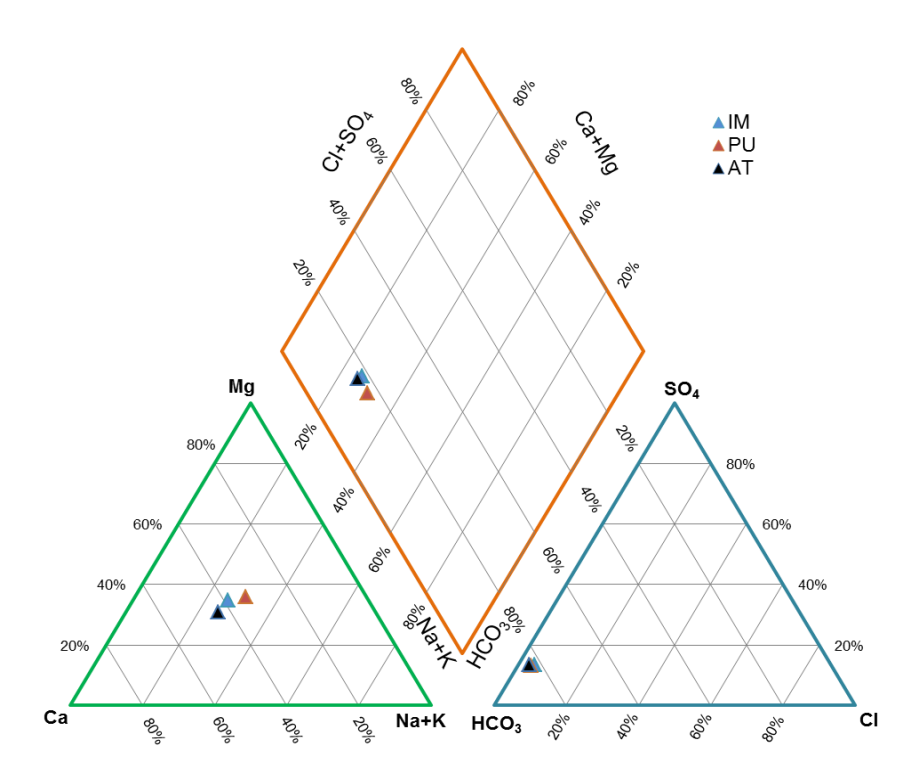


Fig 8. Piper diagram for the dominant composition of anion and cation content.

is the main target for geothermal drilling for electrical energy generation.

4.4 Geochemical analysis

In this study, we also analyzed geochemical data from previous research (Idroes et al., 2019) on several unexplained manifestations, such as those in the Ie Masam, Alue PU, and Alue Teungku areas in the southern volcanic area. The aim is to explain the type of water geothermometer, estimate the depth temperature, and characterize the geothermal water type, specifically using the geochemical analysis data presented in Table 1.

The determination of the dominant chemical composition for the characterization of geothermal water in the Seulawah volcano area was conducted using a piper diagram (Piper, 1944), as depicted in Fig. 8. Based on the diagram, the manifestations of IM, PU, and AT exhibit a chemical composition of sodium–calcium–bicarbonate (Ca–Na–HCO₃). The determination of the geothermal water type is based on the dominant anion content, specifically the bicarbonate water type. In general, the characteristics of bicarbonate water are indicative of immature waters, suggesting that the geothermal water is not in equilibrium. This condition also reflects the influence of surface water mixed with geothermal fluids during

the formation of hot springs (Giggenbach, 1988). The Na/K geothermometer, developed by several researchers with various systematic equations based on the mineral content of Na and K, estimates depth temperature (Giggenbach, 1988). This geothermometer is effective for geothermal fluids with temperatures between 180 and 350°C, and for low temperatures not exceeding 120°C. Table 2 shows the temperature estimates from the depth of manifestation using several Na/K temperature equations (Arnórsson et al., 1983; Fournier, 1979; Giggenbach, 1988; Tonani, 1980).

Based on Table 2, the estimated depth temperatures are consistent with the results from the Na/K geothermometer. The estimated depth temperatures for the manifestations at Ie Masam, Alue PU, and Alue Teungku are $333.1 \pm 27.9^{\circ}$ C,, $302.1 \pm 21.4^{\circ}$ C,, and $276.4 \pm 17.5^{\circ}$ C,, respectively. All these manifestations are located in the southern zone of Mount Seulawah, with the dominant geothermal water content being bicarbonate ions, similar to the Ie-Brôuk manifestation in the northern zone. According to Hochstein & Sudarman (2008), the dominant bicarbonate manifestation results from the formation of CO₂ during the gas and steam condensation process, which leads to the formation of underground hot springs generally found on the slopes of volcanoes with high-temperature water conditions. Fig. 9 displays some documentation of the

 Table 2

 Geothermometer equation for temperature estimation of the depth of manifestation

Location	Na/K Fournier (1979) (°C)	Na/K Tonani (1980) (°C)	Na/K Arnorsson (1983) (°C)	Na/K Giggenbach (1988) (°C)
Ie Masam	315.9	374.7	318.9	322.7
Alue PU	290.3	333.0	285.6	299.6
Alue Teungku	268.6	298.9	258.0	279.9



Fig 9. Documentation of various traces of manifestations in the Seulawah Agam volcano, (a) in the form of a hot spring in Ie Jue and, (b) in the form of warm ground, where in general there are two craters on the north and south sides, namely (c) Heutz crater, which is close to the peak, and (d) is the fumarole, which is also close to the Heutz crater.

manifestations of Seulawah Agam, such as hot springs which are marked by the emergence of geothermally heated groundwater to the Earth's surface, and warm ground, which has a high temperature due to volcanic gases and high-temperature water vapor rising to the surface. Generally, temperatures in the Ie Jue and Ie Seum areas range from 30°C to 40°C. Additionally, there are also two craters in the volcanic area, namely Heutz and Cempaga, where there are fumaroles as volcanic gas that are predominantly water vapor such as carbon dioxide and sulfur dioxide, hydrogen chloride, and hydrogen sulfide.

7. Conclusion

We used the transient electromagnetic method to determine the shallow structure of the Seulawah Agam geothermal area in greater detail. Measurements were taken at 60 points, covering the entire volcanic area, with a distance of 500 m between each point. Several manifestations in the research area indicate an existing structure that serves as a medium for transferring hot fluids to the Earth's surface. The analyzed data is then inverted to create subsurface models in 1D, pseudo-2D, and pseudo-3D

formats, revealing the horizontal distribution of resistivity anomalies. The results show that high resistivity values, ranging from 280.63 to 2542.4 Ω m, are likely due to basalt rock at a depth of 0 to 200 m. Furthermore, the first layer is presumed to consist of volcanic deposits with lower resistivity, especially in the valleys. Additionally, a conductive zone, identified as a clay cap, is present in the second layer with resistivity values of less than 13 Ωm. The lowest layer displays moderate resistivity values ranging from 9.56 to 165.04 Ωm, suggesting the presence of rocks with potential as geothermal reservoirs. From the 2D model, the resistivity contrast indicates the possible presence of local faults around the volcanic area, some of which are close to the manifestations. This is also supported by geological data, which identifies faults in the area. The horizontal distribution of resistivity values, analyzed from the pseudo-3D model, shows a low anomaly at shallow depths (<100 m) in the northern part of the study area, where manifestations are located. Between depths of 200 to 1000 m, a conductive layer dominated by the clay cap is present, while at depths greater than 1000 m, the area is dominated by reservoir rocks, which are the main targets for geothermal exploration. Based on geochemical analysis, the

temperature at Seulawah Agam indicates that the volcano has the potential for high-enthalpy geothermal development.

Acknowledgments

The authors thank the Energy and Mineral Resources Agency of Aceh Province for providing support regarding the geological data of Seulawah Agam. Thanks also to Elnusa Tbk for permission to use software inversion and analyze MT and TEM data, while Mr. Ahmad Al-Farabi Nasution for their help in the inversion process of TEM data.

Funding: This study was funded by the Research Grants of Terapan Unggulan Perguruan Tinggi from the Indonesian Ministry of Education, Culture, Research and Technology in 2022 with the contract: 16/UN11.2.1/PT.01.03/DRPM/2022.

Conflicts of Interest: The authors declare that they have no conflict of interest in this paper.

References

- Abdullah, F., Yanis, M., Razi, M. H., Zainal, M., & Ismail, N. (2022). Subsurface mapping of fault structure in the Weh island by using a 3D density of global gravity. *International Journal of Geomate*, 23(96), 121–128. https://doi.org/10.21660/2022.96.3354
- Arnórsson, S., Gunnlaugsson, E., & Svavarsson, H. (1983). The chemistry of geothermal waters in Iceland. III. Chemical geothermometry in geothermal investigations. *Geochimica et Cosmochimica Acta*, 47(3), 567–577. https://doi.org/10.1016/0016-7037(83)90278-8
- Bennett, J. D., Bridge, N. R., Djunuddin, A., Ghazali, S. A., Jeffery, D. H., Keats, W., Rock, N. M. S., Thompson, S. J., & Whandoyo, R. (1981). The Geology of the Banda Aceh Quadrangle, Sumatra-Geological Research and Development Centre, Bandung. Explanatory Note, 19.
- Chambefort, I., Buscarlet, E., Wallis, I. C., Sewell, S., & Wilmarth, M. (2016). Ngatamariki Geothermal Field, New Zealand: Geology, geophysics, chemistry and conceptual model. *Geothermics*, 59, 266–280. https://doi.org/10.1016/j.geothermics.2015.07.011
- Chave, A. D., & Jones, A. G. (2012). The magnetotelluric method: Theory and practice. In *The Magnetotelluric Method: Theory and Practice*. https://doi.org/10.1017/CBO9781139020138
- Constable, S. C., Parker, R. L., & Constable, C. G. (1987). Occam's inversion: a practical algorithm for generating smooth models from electromagnetic sounding data. *Geophysics*, 52(3), 289–300. https://doi.org/10.1190/1.1442303
- Demissie, Y. (2005). Transient Electromagnetic Resistivity Survey at the Geysir Geothermal Field South Iceland. World Geothermal Congress 2005, April.
- Erfurt-Cooper, P. (2011). Geotourism in volcanic and geothermal environments: Playing with fire? *Geoheritage*, 3(3), 187–193. https://doi.org/10.1007/s12371-010-0025-6
- Fitterman, D. V, & Stewart, M. T. (1986). Transient electromagnetic sounding for groundwater. *Geophysics*, 51(4), 995–1005.
- Fournier, R. O. (1979). A revised equation for the Na/K geothermometer. *Transactions of the Geothermal Resources Council*, 3, 221–224.
- Giggenbach, W. F. (1988). Geothermal solute equilibria. Derivation of Na-K-Mg-Ca geoindicators. *Geochimica et Cosmochimica Acta*, 52(12), 2749–2765. https://doi.org/10.1016/0016-7037(88)90143-3
- Hartono, D., Hastuti, S. H., Halimatussadiah, A., Saraswati, A., Mita, A. F., & Indriani, V. (2020). Comparing the impacts of fossil and renewable energy investments in Indonesia: A simple general equilibrium analysis. *Heliyon*, 6(6). https://doi.org/10.1016/j.heliyon.2020.e04120
- Hochstein, M. P., & Sudarman, S. (1993). Geothermal resources of

- Sumatra. *Geothermics*, 22(3), 181–200. https://doi.org/10.1016/0375-6505(93)90042-L
- Hochstein, M. P., & Sudarman, S. (2008). History of geothermal exploration in Indonesia from 1970 to 2000. *Geothermics*, 37(3), 220–266. https://doi.org/10.1016/j.geothermics.2008.01.001
- Hördt, A., Jödicke, H., Strack, K. -M, Vozoff, K., & Wolfgram, P. A. (1992). Inversion of long-offset TEM soundings near the borehole Münsterland 1, Germany, and comparison with MT measurements. *Geophysical Journal International*, 108(3), 930–940. https://doi.org/10.1111/j.1365-246X.1992.tb03481.x
- Huenges, E. (2010). Geothermal energy systems: esploration, development, and utilization (P. Ledru (ed.)). John Wiley & Sons.
- Idroes, R., Yusuf, M., Saiful, S., Alatas, M., Subhan, S., Lala, A., Muslem, M., Suhendra, R., Idroes, G. M., Marwan, M., & Mahlia, T. M. I. (2019). Geochemistry exploration and geothermometry application in the North Zone of Seulawah Agam, Aceh Besar District, Indonesia. *Energies*, 12(23). https://doi.org/10.3390/en12234442
- Ismail, N., Yanis, M., Idris, S., Abdullah, F., & Hanafiah, B. (2017). Near-Surface Fault Structures of the Seulimuem Segment Based on Electrical Resistivity Model. *Journal of Physics: Conference Series*, 846(1), 012016. https://doi.org/10.1088/1742-6596/846/1/012016
- Ledo, J., García-Merino, M., Larnier, H., Slezak, K., Piña-Varas, P., Marcuello, A., Queralt, P., Pérez, N. M., Schmincke, H. U., & Sumita, M. (2021). 3D electrical resistivity of Gran Canaria island using magnetotelluric data. *Geothermics*, 89. https://doi.org/10.1016/j.geothermics.2020.101945
- Li, H., Xue, G. qiang, Zhou, N. nan, & Chen, W. ying. (2015). Appraisal of an Array TEM Method in Detecting a Mined-Out Area Beneath a Conductive Layer. *Pure and Applied Geophysics*, 172(10), 2917–2929. https://doi.org/10.1007/s00024-015-1075-0
- Lichoro, C. M., Árnason, K., & Cumming, W. (2017). Resistivity imaging of geothermal resources in northern Kenya rift by joint 1D inversion of MT and TEM data. *Geothermics*, 68, 20–32. https://doi.org/10.1016/J.GEOTHERMICS.2017.02.006
- Marwan, Idroes, R., Yanis, M., Idroes, G. M., & Syahriza. (2021). A Low-Cost UAV Based Application for Identify and Mapping A Geothermal Feature in Ie Jue Manifestation, Seulawah Volcano, Indonesia. *International Journal of Geomate*, 20(80), 135–142. https://doi.org/10.21660/2021.80.j2044
- Marwan, M., Asrillah, Yanis, M., & Furumoto, Y. (2019). Lithological identification of devastated area by Pidie Jaya earthquake through poisson's ratio analysis. *International Journal of GEOMATE*, 17(63), 210–216. https://doi.org/10.21660/2019.63.77489
- Marwan, M., Yanis, M., Nugraha, G. S., Zainal, M., Arahman, N., Idroes, R., Dharma, D. B., Saputra, D., & Gunawan, P. (2021). Mapping of Fault and Hydrothermal System beneath the Seulawah Volcano Inferred from a Magnetotellurics Structure. *Energies*, 14(19), 6091. https://doi.org/10.3390/en14196091
- Marwan, Syukri, M., Idroes, R., & Ismail, N. (2019). Deep and shallow structures of geothermal Seulawah Agam based on electromagnetic and magnetic data. *International Journal of GEOMATE*, 16(53), 141–147. https://doi.org/10.21660/2019.53.17214
- Marwan, Yanis, M., Idroes, R., & Ismail, N. (2019). 2D inversion and static shift of MT and TEM data for imaging the geothermal resources of Seulawah Agam Volcano, Indonesia. *International Journal of GEOMATE*, 17(62). https://doi.org/10.21660/2019.62.11724
- Marwan, Yanis, M., Muzakir, & Nugraha, G. S. (2020). Application of QR codes as a new communication technology and interactive tourist guide in Jaboi, Sabang. IOP Conference Series: Materials Science and Engineering, 796(1), 012025. https://doi.org/10.1088/1757-899X/796/1/012025
- McNeill, J. D. (1980). Applications of transient electromagnetic techniques. Geonics Limited Missasauga, ON, Canada.
- Mohan, K., Chaudhary, P., Kumar, G. P., Kothyari, G. C., Choudhary, V., Nagar, M., Patel, P., Gandhi, D., Kushwaha, D., & Rastogi, B. K. (2018). Magnetotelluric Investigations in Tuwa-Godhra Region, Gujarat (India). *Pure and Applied Geophysics*, 175(10), 3569–3589. https://doi.org/10.1007/s00024-018-1883-0

- Montecinos-Cuadros, D., Díaz, D., Yogeshwar, P., & Munoz-Saez, C. (2021). Characterization of the shallow structure of El Tatio geothermal field in the Central Andes, Chile using transient electromagnetics. *Journal of Volcanology and Geothermal Research*, 412, 107198. https://doi.org/10.1016/j.jvolgeores.2021.107198
- Moya, D., Aldás, C., & Kaparaju, P. (2018). Geothermal energy: Power plant technology and direct heat applications. In *Renewable and Sustainable Energy Reviews* (Vol. 94, pp. 889–901). https://doi.org/10.1016/j.rser.2018.06.047
- Nasruddin, Idrus Alhamid, M., Daud, Y., Surachman, A., Sugiyono, A., Aditya, H. B., & Mahlia, T. M. I. (2016). Potential of geothermal energy for electricity generation in Indonesia: A review. In *Renewable and Sustainable Energy Reviews* (Vol. 53, pp. 733–740). https://doi.org/10.1016/j.rser.2015.09.032
- Nugraha, G. S., Ebubakar, M., Alawiyah, S., & Sutopo. (2016). Geological Structure Causes of the Rise in Burni Telong Manifestations, Bener Meriah, Central Aceh, Indonesia. *Electronic journal of geothecinal engineering*, 21(1), 201–210.
- Peacock, J. R., Mangan, M. T., McPhee, D., & Wannamaker, P. E. (2016). Three-dimensional electrical resistivity model of the hydrothermal system in Long Valley Caldera, California, from magnetotellurics. *Geophysical Research Letters*, 43(15), 7953– 7962. https://doi.org/10.1002/2016GL069263
- Piper, A. M. (1944). A graphic procedure in the geochemical interpretation of water-analyses. *Eos, Transactions American Geophysical Union*, *25*(6), 914–928. https://doi.org/10.1029/TR0251006P00914
- Purnomo, B. J., & Pichler, T. (2014). Geothermal systems on the island of Java, Indonesia. *Journal of Volcanology and Geothermal Research*, 285, 47–59. https://doi.org/10.1016/j.jvolgeores.2014.08.004
- Rizal, M., Ismail, N., Yanis, M., Muzakir, & Surbakti, M. S. (2019). The 2D resistivity modelling on north sumatran fault structure by using magnetotelluric data. *IOP Conference Series: Earth and Environmental Science*, 364(1). https://doi.org/10.1088/1755-1315/364/1/012036
- Ruiz-Aguilar, D., Tezkan, B., & Arango-Galván, C. (2018). Exploration of the Aquifer of San Felipe Geothermal Area (Mexico) by Spatially Constrained Inversion of Transient Electromagnetic Data. *Journal of Environmental and Engineering Geophysics*, 23(2), 197–209. https://doi.org/10.2113/JEEG23.2.197
- Ruiz-Aguilar, D., Tezkan, B., Arango-Galván, C., & Romo-Jones, J. M. (2020). 3D inversion of MT data from northern Mexico for geothermal exploration using TEM data as constraints. *Journal of Applied Geophysics*, 172. https://doi.org/10.1016/j.jappgeo.2019.103914
- Ruthsatz, A. D., Sarmiento Flores, A., Diaz, D., Reinoso, P. S., Herrera, C., & Brasse, H. (2018). Joint TEM and MT aquifer study in the Atacama Desert, North Chile. *Journal of Applied Geophysics*, *153*, 7–16. https://doi.org/10.1016/J.JAPPGEO.2018.04.002
- Rybach, L. (2003). Geothermal energy: Sustainability and the environment. *Geothermics*, *32*(4), 463–470. https://doi.org/10.1016/S0375-6505(03)00057-9
- Saptadji, N. M. (2001). Teknik Panasbumi. Penerbit ITB.
- Sieh, K., & Natawidjaja, D. (2000). Neotectonics of the Sumatran fault, Indonesia. *Journal of Geophysical Research: Solid Earth*, 105(B12), 28295–28326. https://doi.org/10.1029/2000jb900120
- Siripunvaraporn, W., & Egbert, G. (2009). WSINV3DMT: Vertical magnetic field transfer function inversion and parallel implementation. *Physics of the Earth and Planetary Interiors*, 173(3– 4), 317–329. https://doi.org/10.1016/j.pepi.2009.01.013
- Spies, B. R. (1989). Depth of investigation in electromagnetic sounding methods. *Geophysics*, 54(7), 872–888. https://doi.org/10.1190/1.1442716
- Strack, K. M. (1992). Exploration with deep transient electromagnetics (Vol.373). Elsevier.
- Telford, M. ., Telford, W. M., Geldart, L. P., & Sheriff, R. E. (1990).

- Applied Geophysics. In *Applied Geophysics* (Vol. 127, Issue 3212). Cambridge University Press. USA. https://doi.org/10.1017/cbo9781139167932
- Tonani, F. B. (1980). Some remarks on the application of geochemical techniques in geothermal exploration. In *Advances in European Geothermal Research* (pp. 428–443). Springer.
- Vozoff, K. (1980). Electromagnetic methods in applied geophysics. *Geophysical Surveys*, 4(1–2), 9–29. https://doi.org/10.1007/BF01452955
- Wang, G. ling, Zhang, W., Ma, F., Lin, W. jing, Liang, J. yun, & Zhu, X. (2018). Overview on hydrothermal and hot dry rock researches in China. *China Geology*, 1(2), 273–285. https://doi.org/10.31035/cg2018021
- Yanis, M., A Bakar, M., & Ismail, N. (2017, September). The Use of VLF-EM and Electromagnetic Induction Methods for Mapping the Ancient Fort of Kuta Lubok as Tsunami Heritage i. 23rd European Meeting of Environmental and Engineering Geophysics. https://doi.org/10.3997/2214-4609.201701996
- Yanis, M., Abdullah, F., Zaini, N., & Ismail, N. (2021). The northernmost part of the Great Sumatran Fault map and images derived from gravity anomaly. *Acta Geophysica*, *69*(3), 795–807. https://doi.org/10.1007/s11600-021-00567-9
- Yanis, M., Faisal, A., Yenny, A., Muzakir, Z., Abubakar, M., & Nazli, I. (2020). Continuity of Great Sumatran Fault in the Marine Area revealed by 3D Inversion of Gravity Data. *Jurnal Teknologi*, 83(1), 145–155. https://doi.org/10.11113/jurnalteknologi.v83.14824
- Yanis, M., Ismail, N., & Abdullah, F. (2022). Shallow Structure Fault and Fracture Mapping in Jaboi Volcano, Indonesia, Using VLF–EM and Electrical Resistivity Methods. *Natural Resources Research*, 31(1), 335–352. https://doi.org/10.1007/s11053-021-09966-7
- Yanis, M., Marwan, Idroes, R., Zaini, N., Paembonan, A. Y., Ananda, R., & Ghani, A. A. (2022). A pilot survey for mapping the fault structure around the Geuredong volcano by using high-resolution global gravity. Acta Geophysica 2022, 1–19. https://doi.org/10.1007/S11600-022-00860-1
- Yanis, M., Marwan, M., Paembonan, A. Y., Yudhyantoro, Y., Rusydy, I., Idris, S., & Asrillah, A. (2021). Geophysical and Geotechnical Approaches in Developing Subsurface Model for Gas Power Plant Foundation. *Indian Geotechnical Journal*. https://doi.org/10.1007/s40098-021-00559-y
- Yanis, M., Novari, I., Zaini, N., Marwan, Pembonan, A. Y., & Nizamuddin. (2020). OLI and TIRS Sensor Platforms for Detection the Geothermal Prospecting in Peut Sagoe Volcano, Aceh Province, Indonesia. Proceedings of the International Conference on Electrical Engineering and Informatics, 2020-Octob, 1–6. https://doi.org/10.1109/ICELTICs50595.2020.9315378
- Yanis, M., Zainal, M., Marwan, M., & Ismail, N. (2019, June 3). Delineation of Buried Paleochannel Using EM Induction in Eastern Banda Aceh, Indonesia. 81st EAGE Conference and Exhibition 2019. https://doi.org/10.3997/2214-4609.201900705
- Yanis, M., Zaini, N., Novari, I., Abdullah, F., Dewanto, B. G., Isa, M., Marwan, M., Zainal, M., & Abdurrahman, A. (2023). Monitoring of Heat Flux Energy in the Northernmost Part of Sumatra Volcano Using Landsat 8 and Meteorological Data. *International Journal of Renewable Energy Development*, 12(1), 55–65. https://doi.org/10.14710/ijred.2023.47048
- Zaini, N., Yanis, M., Abdullah, F., Van Der Meer, F., & Aufaristama, M. (2022). Exploring the geothermal potential of Peut Sagoe volcano using Landsat 8 OLI/TIRS images. *Geothermics*, 105, 102499. https://doi.org/10.1016/j.geothermics.2022.102499
- Zaini, N., Yanis, M., Marwan, Isa, M., & van der Meer, F. (2021). Assessing of land surface temperature at the Seulawah Agam volcano area using the landsat series imagery. *Journal of Physics:* Conference Series, 1825(1). https://doi.org/10.1088/1742-6596/1825/1/012021
- Zhdanov, M. S. (2009). Geophysical electromagnetic theory and methods (First Edit). Elsevier B.V. https://doi.org/10.1016/s0076-6895(09)70001-0



© 2025. The Author(s). This article is an open access article distributed under the terms and conditions of the Creative Commons Attribution-ShareAlike 4.0 (CC BY-SA) International License (http://creativecommons.org/licenses/by-sa/4.0/)